LANGMUIR

pubs.acs.org/Langmuir Article

Influence of Surface Ligand Molecular Structure on Phospholipid Membrane Disruption by Cationic Nanoparticles

Yongqian Zhang,[⊥] Udaya Dahal,[⊥] Z. Vivian Feng, Zeev Rosenzweig, Qiang Cui, and Robert J. Hamers*

Cite This: https://doi.org/10.1021/acs.langmuir.1c01146 Read Online

ACCESS | Metrics & More | Article Recommendations | Supporting Information

ABSTRACT: Cationic nanoparticles are known to interact with biological membranes and often cause serious membrane damage. Therefore, it is important to understand the molecular mechanism for such interactions and the factors that impact the degree of membrane damage. Previously, we have demonstrated that spatial distribution of molecular charge at cationic nanoparticle surfaces plays an important role in determining the cellular uptake and membrane damage of these nanoparticles. In this work, using diamond nanoparticles (DNPs) functionalized with five different amine-based surface ligands and small phospholipid unilamellar vesicles (SUVs), we further investigate how chemical features and conformational flexibility of surface ligands impact nanoparticle/membrane interactions. ^{31}P-NMR T_2 relaxation measurements quantify the mobility changes in lipid dynamics upon exposing the SUVs to functional DNPs, and coarse-grained molecular dynamics simulations further elucidate molecular details for the different modes of DNP−SUV interactions depending on the surface ligands. Collectively, our results show that the length of the hydrophobic segment and conformational flexibility of surface ligands are two key factors that dictate the degree of membrane damage by the DNP, while the amount of surface charge alone is not predictive of the strength of interaction.

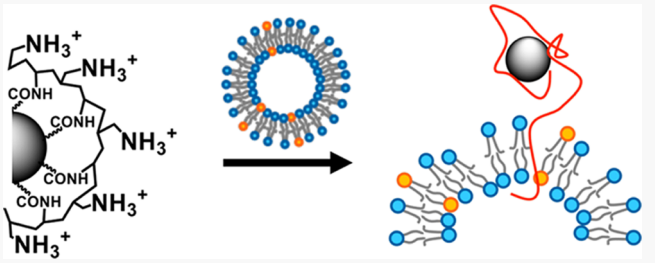

INTRODUCTION

Surface charge plays a critical role in maintaining the colloidal stability of nanoparticles (NPs) and controlling their interactions with the surroundings.[1] Therefore, modulating the properties of these surface-charged groups is key to control the reactivity, biocompatibility, and biological responses of functionalized NPs. Prior studies have established that positively charged (cationic) functional groups at NP surfaces induce significantly stronger cell interaction and internalization compared to neutral or negatively charged (anionic) groups[2,3] due to favorable electrostatic interactions between the NPs and cell surfaces, which are typically negatively charged. Current strategies of controlling the NP−cell interactions are limited and mainly focus on tuning the charge density,[4,5] functional groups,[1] and the overall hydrophobicity[6,7] of the NP surfaces. A few number of studies have shown that variations in conformation[8] and ligand arrangement[9] of the molecular layer at NP surfaces lead to different cellular uptakes and membrane interactions; these studies suggest that presentation of the surface molecular layers plays an important role in nanoparticle−cell interactions.

One key challenge to developing a molecular-level understanding of how the conformation and presentation of NP surface charge impact cell interactions is that on most NPs studied previously, the molecular surface layers can be easily removed or displaced under biological conditions.[10−12] As a result, the actual surface chemical composition at the time of interaction is largely unknown. Diamond nanoparticles (DNPs) provide a robust platform to investigate the impact of surface features since it is possible to functionalize their surfaces with diverse ligands via covalent interactions.[13−16] Taking advantage of this unique advantage of DNPs, we demonstrated that the spatial distribution and presentation of charged groups play a key role in determining NP−cell interactions, regardless of their ζ potential and identity of the cationic functional groups.[17] Specifically, the positive charges carried by linear molecular ligands show minimal interactions with the cell membrane, while cationic polymer ligands lead to significant membrane interactions.[17]

Here, we present a combined experimental and computational study to demonstrate how the conformation and presentation of charged functional groups at DNP surfaces impact their interactions with model phospholipid membranes. Figure 1 shows the five cationic DNP surfaces that we designed, including four surfaces modified with linear molecules bearing terminal surface charges and one surface covalently linked to a cationic polymer. DNPs functionalized with a primary amine and quaternary amine via a short

Received: April 27, 2021
Revised: May 22, 2021

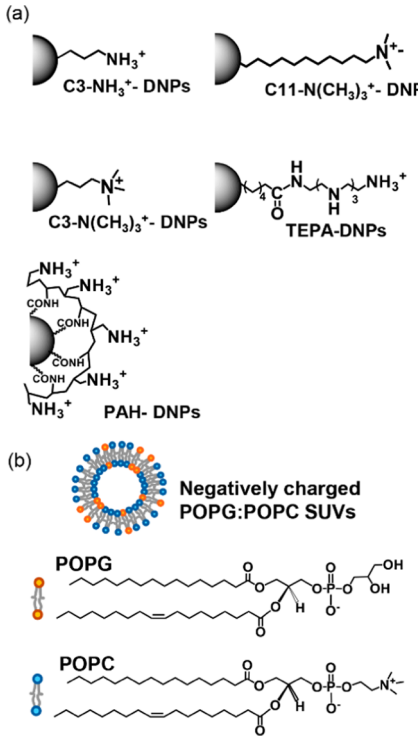

Figure 1. Scheme of (a) four DNPs functionalized with linear molecular ligands and one functionalized with PAH polymers and (b) negatively charged palmitoyl-oleoyl phosphatidyl glycerol (POPG)/Palmitoyl-oleoyl phosphatidyl choline (POPC) SUVs used in this study.

aliphatic chain (C3) were designed to identify the influence of amino functional groups. DNPs functionalized with a longer aliphatic chain (C11) terminated with tetramethylammonium group (C11-$N(CH_3)_3^+$-DNPs) are designed to explore the influence of hydrophobic chain length. DNPs functionalized with tetraethylenepentamine (TEPA−DNPs) were prepared to determine the influence of charges distributed along the length of the molecules. Finally, DNPs functionalized with poly-(allylamine) (PAH−DNPs) via covalent linkage were prepared to determine the influence of ligand conformational flexibility. We used phospholipid small unilamellar vesicles (SUVs) as a model membrane, as commonly done in the literature.[18−21] A fluorescence-based SUV lysis assay determines the membrane damage upon amino DNP exposure and shows that PAH−DNPs induce the highest degree of membrane damage. Furthermore, ^{31}P-NMR T_2 relaxation measurements combined with coarse-grained (CG) molecular dynamic simulations were used to probe changes in the SUV membrane at the molecular level upon exposure to amino-functionalized DNPs. Our results show that the molecular ligand-functionalized DNPs and polymer−DNPs induce different degrees of membrane damages with distinct interactions. PAH−DNP induces a high degree of membrane damage by penetrating deeply into phospholipid layers via the highly mobile poly(allylamine hydrochloride) (PAH) chains extending away from DNP surfaces. By contrast, DNPs functionalized with linear molecular ligands induce much weaker interactions by either adsorbing at the membrane surfaces via electrostatic interactions or inducing lipid extraction. Our study demonstrates that compared to short conformationally rigid surface groups, long conformationally flexible groups at nanoparticle surfaces intercalate much more effectively into phospholipid membranes. Thus, the conformational flexibility of surface ligands is a key factor that controls the biological impact of cationic-functionalized nanoparticles. While demonstrated here for molecules having well-defined structures, we anticipate that factors probed here may also be important in understanding how other types of nanoparticle molecular coatings, such as protein coronas, induce a molecule-specific biological response.

EXPERIMENTAL SECTION

Materials and Functionalized Diamond Nanoparticles (DNPs). Nanopure water (Barnsted Nanopure system, resistivity ≥ 18 MΩ·cm) was used for all experiments. Diamond nanoparticles were functionalized using a radical-based grafting method described previously.[16] Detailed characterization using X-ray photoelectron spectroscopy, ^{1}NMR, and dynamic light scattering is described in the SI. Figure 1a shows the scheme of the five cationic diamond nanoparticles (DNPs) that are functionalized with short molecular ligands (C3-NH_3^+ and C3-$N(CH_3)_3^+$), long molecular ligands (C11-$N(CH_3)_3^+$ and TES), and polymer (PAH). Dimethyl vinylphosphonate (>95%, GC, Millipore Sigma) was used to functionalize DNPs (^{31}P-DNPs) as a control for the T_2 relaxation NMR experiments. Palmitoyl-oleoyl phosphatidyl choline (POPC), palmitoyl-oleoyl phosphatidyl glycerol (POPG), and 50 nm pore-size polycarbonate filters (for separating and purifying vesicles) were purchased from Avanti Polar Lipids. Figure 1b shows the scheme and chemical structure of a small unilamellar vesicle (SUV) that is made with POPC and POPG lipids.

Preparation of POPG/POPC SUVs. We prepared vesicles of mixed POPG/POPC composition following literature methods that produce small unilamellar vesicles with an overall diameter of 50−100 nm.[21,22] After the POPG and POPC lipids were mixed at a 1:9 molar ratio in a round-bottom flask, the phospholipid mixture was dried under a nitrogen stream while rotating the flask to form an even and thin layer of lipid film on the bottom of the round-bottom flask. The phospholipid mixture was further dried under a nitrogen stream or vacuum overnight to completely remove the chloroform.

Preparation of POPG/POPC SUVs for the Fluorescence Leakage Assay. Dried phospholipid films were resuspended in 2 mL of 10 mM MES buffer with calcein (25 mM). Droplets of NaOH solution (2 M) were added to the phospholipid−calcein buffer solution until the calcein dye was fully dissolved. The final solution exhibits a dark red-orange color and was subsequently freeze−thawed in a microcentrifuge tube between liquid nitrogen and a 20 °C water bath a minimum of 10 times. The phospholipid vesicles were broken down into smaller unilamellar vesicles by extrusion (at least 20 times) using a polycarbonate membrane with a pore size of 50 nm; the resulting solution was clear (red-orange color). These SUVs were further purified using size exclusion column chromatography to separate the calcein-encapsulated SUVs from the excess-free calcein dyes. In this step, 400 μL of the extruded SUV suspension was loaded onto a Sepharose CL-4B column (10 mm × 100 mm) and was eluted with 10 mM MES buffer. The calcein-encapsulated SUVs elute before the free calcein and appear as a faint brown-orange band in the column. The purified calcein-encapsulated SUV solution was diluted 1000 times in 10 mM MES buffer (50 μL SUVs in 50 mL buffer). We found that leaving samples for 1 day in ambient illumination yielded lower fluorescence from dye molecules in the aqueous medium outside the vesicles and therefore adopted this 1 day stabilization as part of our procedure.

Preparation of POPG/POPC SUVs for the ^{31}P-T_2 NMR Experiment. The dried phospholipid film was resuspended in 2 mL of 10 mM MES buffer. The final solution exhibits an opaque milky color and was subsequently freeze−thawed in a microcentrifuge tube between liquid nitrogen and a 20 °C water bath a minimum of 10 times. The phospholipid vesicles were broken down into smaller unilamellar vesicles by extrusion (at least 20 times) using a polycarbonate membrane with a pore size of 50 nm, and the resulting solution should be clear (white color). The purified POPG/POPC

https://doi.org/10.1021/acs.langmuir.1c01146
Langmuir XXXX, XXX, XXX−XXX

Table 1. Compositions of Functionalized Nanodiamonds (DNPs) Studied with the BMW-MARTINI Model

materials	bead type	no. of ligands	total ligand charge (e)
LA−DNPs	3C1 + 1Q_d (+1e)	138	+138
SA−DNPs	1C1 + 1Q_0 (+1e)	138	+138
TEPA−DNPs	2P5 + P5(+1e) 1Q_d (+1e)	138	+276
PAH−DNPs	1C1 + 1Q_d (+1e)	8 (PAH_{20}), 16 (PAH_{20})	+160, +320
untreated DNPs	P4		0

SUVs were characterized by dynamic light scattering and micro-electrophoretic light scattering, and our results show that the purified POPG/POPC SUV is 51 ± 12 nm and carries a negative ζ potential of −9.2 ± 1.2 mV.

Evaluation of SUV Lysis toward Functionalized DNPs. To evaluate the membrane damage of five different cationic-functionalized DNPs, we used a fluorescence-based method to quantify the membrane damage of the phospholipid SUVs.[22,23] Steady-state and time-resolved fluorescence measurements were collected with excitation wavelength at 480 nm and emission at 515 nm using a PTI QuantaMaster 300. During the experiment, the fluorescence intensity of 1 mL of the calcein-encapsulated SUVs was measured as the background signal. Once the signal stabilized, 50−60 μL of the stock-functionalized DNP solution was added to the 1 mL calcein-encapsulated SUV solution with final amine concentrations of 10, 20, 40, and 80 nM. Lysis of the SUVs by the functionalized DNPs induces an increase in fluorescence intensity. The signals were monitored until the fluorescence intensity stabilized. Finally, 50 μL of 1% Triton-X-100 was added to the SUV−DNP solution to complete the lysis of SUVs and the fluorescence intensity was recorded until the signal plateaued. All fluorescence results were collected using 1 day old SUVs at room temperature under constant stirring. All fluorescence measurements were repeated at least three times for each sample at each concentration to obtain the average values and error bars. The time-resolved fluorescence curves were analyzed as described previously,[22] and the percentage of phospholipid SUVs lysed was calculated using $\%\text{lysed} = (I_{max} - I_{sample})/(I_{max} - I_{background}) \times 100$. The I_{max} represents the average fluorescence intensity of the maximum SUV lysis, I_{sample} represents the fluorescence intensity of the calcein-encapsulated SUVs upon exposure to functionalized DNPs, and $I_{background}$ represents the fluorescence intensity of the calcein-encapsulated SUVs without NPs.

^{31}P-T_2 Relaxation NMR Experiments. The SUVs that were used for ^{31}P-T_2 relaxation NMR experiments were exposed to each functionalized DNP for 1 h. To archive optimal NMR signals, the extruded SUV solution was only diluted 10 times in D_2O and the amine concentration of the functionalized DNPs was adjusted accordingly to maintain consistency between T_2 measurements and fluorescence-based lysis assay. The ratio between SUV and functionalized DNPs in the final solution is the same as the ratio of those from the fluorescence-based lysis assay with a final amine concentration of 20 nM. All NMR measurements were performed using a Bruker Avance-500 spectrometer with a Prodigy probe. T_2 was measured by the Carr−Purcell−Meiboom−Gill (CPMG) pulse sequence. The relaxation delay (d_1) was set as 7 s, which is more than 3 times longer than the T_1 (measured by the inversion recovery method) of the ^{31}P peaks. All measurements use SUVs that are less than 1 week old and were collected at room temperature with 1500 scans per experiment.

Normalization of SUV Membrane Damage to Amine Concentration. While biological responses to nanomaterials are often plotted versus nanoparticle concentrations, our work aims at understanding the influence of cationic amino functional groups. The amino groups' densities on different functionalized nanoparticles vary with the identity of the ligand. Nanoparticles functionalized with linear molecular ligands carry a smaller number of amino groups compared with DNPs functionalized with cationic polymers. Therefore, to understand whether this inherently higher amine content in PAH−DNPs contributes to the significantly higher SUV membrane damage, we normalized the responses of SUV fluorescence leakage assay using the total concentration of charged amine groups in each sample. We used quantitative ^{1}H NMR to determine the total concentration of amine moieties in each sample and analyzed the SUV membrane damage to show the resulting biological impact for a given concentration of amino groups. This normalization allows us to compare the SUV membrane damage to per amine among different DNP surfaces. For quantitative NMR analysis, three known amounts of each propylamine (with D_2O), propyl trimethylamine (with D_2O), 11-trimethylamine (with D_2O), tetraethylenepentamine (with D_2O), and polyallylamine (with D_2O) were used as external standards, and peak integrations were compared to these standards. Relaxation delay was set to at least 5 times the T_1 of the standards and integrated peak areas are normalized with the number of scans and the receiver gain. The NMR spectra of all samples and corresponding details are included in Zhang et al., 2020[17] since the same batches of the five different amine−DNPs are used.

Molecular Dynamics (MD) Simulations. We studied the interaction between functionalized diamond nanoparticles and SUVs using molecular dynamics simulations and a coarse-grained (CG) MARTINI force field;[24] the choice of a CG model was motivated by the requirement of long simulations to probe the impact of functionalized nanoparticles on the structure and stability of the SUVs. The SUVs studied in the simulation have a composition of 9:1 DLPC/DLPG lipids and contain 920 DLPC lipids and 102 DLPG lipids; the radius is between 6 and 7 nm. At the coarse-grained level, the chemical structures of DLPC and DLPG lipids are essentially identical to those of POPC and POPG lipids (the lipid tail contains one additional double bond for POPC and POPG). Previous analysis demonstrates that the BMW-MARTINI model {Wu, 2010 #52;Wu, 2011 #94} is more consistent with all-atom simulations for the interaction between a cationic nanoparticle and lipid bilayers.[25] Therefore, we used BMW-MARTINI models for this study.

The compositions of the various diamond nanoparticles (DNPs) at the coarse-grained level are summarized in Table 1. Untreated DNPs have oxidized surfaces that are hydrophilic.[15,26] Therefore, we used a set of hydrophilic P4 beads with a core size of 4 nm in diameter for all MD simulations. We also tested the use of P1 bead, which is more hydrophobic than P4; the results (see the Supporting Information) are generally similar. Four different surface ligands were examined in the MD simulation to match experimental conditions, including three molecular ligands and one polymer (PAH). The molecular ligands include (1) long amine (LPA) that contains three hydrophobic beads and one cationic bead, (2) short quaternary amine (SQA) that contains one hydrophobic bead and one cationic bead, and (3) tetraethylenepentamine (TEPA), which contains two polar beads and two charged beads. With coarse-grained simulations, NPs that are functionalized with the short primary amine ligand show identical behaviors as those functionalized with the short quaternary amine (SQA) ligand.[25] For poly(allylamine hydrochloride) (PAH) polymer-functionalized DNP surface, two PAH−DNP models were simulated to explore the influence of conformational flexibility: eight PAH_{20} chains covalently attached on one end to DNPs and eight PAH_{20} chains with both ends covalently anchored to the DNPs. These two models exhibit different ligand conformations and flexibilities at DNP surfaces; they are referred to as the flexible PAH−DNP and rigid PAH−DNP models, respectively.

Each simulation was carried out for at least 1 μs using GROMACS version 2016.3 with an integration time step of 20 femtoseconds. Pressure and temperature were controlled using the Berendsen barostat and thermostat with a coupling time of 4 and 1 ps, respectively. The temperature was maintained at 300 K, pressure at 1

https://doi.org/10.1021/acs.langmuir.1c01146
Langmuir XXXX, XXX, XXX−XXX

bar, and the compressibility was 3×10^5 bar^{-1}. Coulomb interactions were calculated using particle mesh Ewald (PME) with a grid size of ~1 Å, and nonpolar interactions were treated with the tabulated potential developed for BMW-MARTINI with a cutoff distance of 1.4 nm. The system size was approximately 23 nm x 23 nm x 23 nm with 0.15 M NaCl. The SUV was generated using CHARMM-GUI with the established protocol for equilibrating the interior water content.[27] The DNP was set to be 10 Å away from the SUV at the beginning of each simulation.

RESULTS AND DISCUSSION

Impact of Cationic DNPs on POPG/POPC Phospholipid SUVs. We examined the influence of the five different cationic amino-functionalized DNPs on 1:9 POPG/POPC phospholipid SUVs using a fluorescence-based leakage assay and calculating the percentage of SUVs that were lysed.[22,23] Figure 2a shows one representative data set, obtained using a consistent amine concentration of 40 nM in each sample. There are three stages in each curve. During the first stage (shown in the green block), only the calcein-encapsulated SUVs were present; the resulting fluorescence intensities are the smallest and are treated as background signals arising from incomplete self-quenching of the highly concentrated dye molecules encapsulated inside the SUVs. After a stable background was recorded, a solution of functionalized DNPs containing a fixed amount of amine groups was injected into the calcein-encapsulated SUV solution. In this second stage (shown in the yellow background), the data show an initial rapid increase in fluorescence intensity in each curve immediately after the DNPs are injected, followed by a plateau. Finally, Triton-X was added to completely lyse all SUVs. In this third stage, the fluorescence intensity further increases, reaching a single value that is identical for all samples. These data show that the introduction of DNPs into the solution containing SUVs leads to the lysis of a fraction of the SUV. For a fixed amine concentration, the data show that the fraction of SUVs lysed depends significantly on the identity of the surface ligands. A comparison of the data for different surface ligands shows that at the same amine concentration, PAH polymer-functionalized DNPs induced the greatest extent of membrane lysis, followed by DNPs functionalized with long linear ligands (C11-N$(CH_3)_3^+$-DNPs and TEPA–DNPs). The DNPs functionalized with short linear ligands (C3-NH_3^+-DNPs and C3-N$(CH_3)_3^+$-DNPs) induce the lowest lysis.

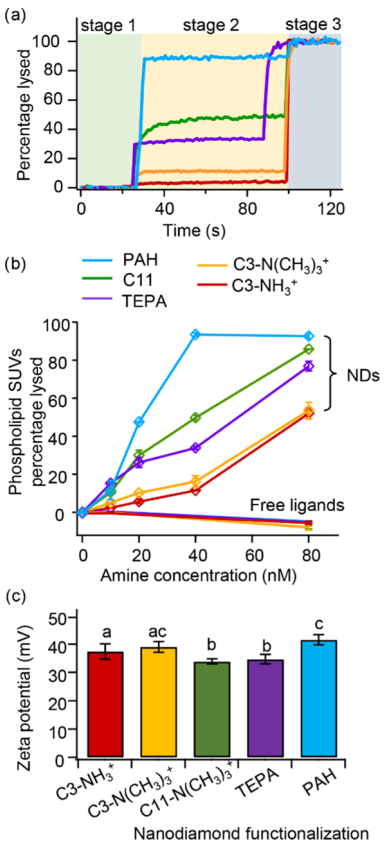

Figure 2. Percentage of lysed phospholipid SUVs upon exposure to DNPs functionalized versus (a) experiment time at 40 nM amine concentration and (b) amine concentration. Some control traces from the free ligand in (b) are not clearly visible due to the overlapping of five traces. Error bars represent 1 standard deviation, $N > 3$ replicates each. (c) ζ potential of functionalized DNPs in 10 mM MES buffer.

Figure 2b shows the quantification results of the final SUV membrane lysis percentage after the SUVs were exposed to the five different amino DNPs at different concentrations of surface-tethered amino groups. Commensurate with Figure 2a, these data show that DNPs functionalized with PAH polymer induce significant damage to SUVs even at low DNP amine concentration (~20 nM) and induce 100% SUV lysis at 40 nM and above. DNPs functionalized with short linear molecular ligands (C3-NH_3^+-DNPs and C3-N$(CH_3)_3^+$-DNPs) induced the least membrane damage across the concentration range studied, while DNPs functionalized with longer linear molecular ligands (C11-N$(CH_3)_3^+$-DNPs and TEPA–DNPs) induced membrane damage to an intermediate extent. Figure 2b also includes control studies that were performed using each of the free molecular ligands; the traces for control samples overlap each other, obscuring visibility of the individual traces. In each case, the free ligands induce only a small change in fluorescence intensity, indicating that the free ligands alone do not exhibit significant membrane damage even at the highest concentration studied. Exposure of the SUVs to the free ligands induces a small decrease in fluorescence intensity, leading to a level of apparent membrane damage that is slightly negative. Based on the above data, we conclude that the lysis of SUV membranes by the amino groups occurs only when the ligands are linked to the nanoparticle surfaces. Overall, the data in Figure 2 show that the amino groups present in a polymer (such as PAH) induce much stronger membrane interactions compared with the amino groups at the same concentration that are present in linear ligands that are tethered more closely to the DNP surfaces. Our data also show that primary and quaternary amines have similar effects, indicating that the precise chemical nature of the charged groups has only a minor impact on the interaction with the membrane. Finally, we note that while we present our data using a fixed concentration of DNP-tethered amino groups in Figure 2b and as the independent variable in Figure 2c, the PAH-modified DNPs have the largest number of amino groups per nanoparticle (Supporting Information). Consequently, if we had instead presented these data as a function of nanoparticle concentration instead of amino concentration, the stronger interaction of PAH–DNPs would be even more dramatic.

Since most biological membranes have a net negative charge, the interaction of positively charged nanoparticles is frequently attributed primarily to electrostatic interactions.[1,3] The net surface charge is frequently assessed using measurements of

https://doi.org/10.1021/acs.langmuir.1c01146
Langmuir XXXX, XXX, XXX–XXX

the ζ potential (ζ potential).[22,28,29] Figure 2c shows the ζ potentials of the five cationic surfaces in 10 mM MES buffer (SUV media). These data show that ζ potentials of the DNPs functionalized with the linear molecular ligand are very similar to those of DNPs functionalized with polymer (PAH−DNPs), except that the C11-N$(CH_3)_3^+$-DNPs and TEPA−DNPs exhibit slightly smaller ζ potentials. As discussed in our recent work, the ζ potential may not accurately reflect the surface charge due to the compensation of counterions. {Liang, 2020 #512} Yet, we find that on a "per amine" basis, the polymer-modified DNPs (PAH−DNPs), DNPs modified with long linear ligands (C11-N$(CH_3)_3^+$-DNPs and TEPA−DNPs), and DNPs modified with short linear ligands (C3-NH_3^+-DNPs and C3-N$(CH_3)_3^+$-DNPs) all exhibit significantly different membrane interactions. A comparison of the membrane damage data in Figure 2b with the ζ potential data in Figure 2c shows that neither the concentration of DNP-tethered amino groups nor the ζ potential is predictive of the membrane damage induced by exposure to functionalized nanoparticles.

Based on the above observations, we hypothesize that the structure and conformational flexibility of surface ligands play important roles in controlling the DNP−membrane interaction. In prior work, we used ^{1}H NMR T_2 measurements to characterize the molecular conformations and relaxation dynamics of PAH-modified DNP prepared via a different synthesis route.[30] Those studies revealed two distinct populations, one arising from polymer segments close to the DNP surface and a second corresponding to highly flexible segments extending into the aqueous medium.[30] Similar conformations have been reported for other polymers at planar and nanoparticle surfaces,[31,32] with loops and exposed tails extending into the adjacent liquid medium.[33−35] Since in the present work we use a different method to covalently link PAH to DNP surfaces, we measured the new PAH−DNPs with ^{1}H-T_2 measurements. Consistent with our prior work, our present NMR studies show two distinct populations, one corresponding to sites rigidly bonded to the surface (~70 ± 5% of all ^{1}H) and a second population associated with highly flexible polymer loops and tails (~30 ± 5%) (details in the Supporting Information). We hypothesize that as the length of the ligand increases, the conformational flexibility of ligands changes, resulting in different DNP−membrane interactions. Specifically, we attribute the high membrane damage of PAH−DNPs and the lower membrane damage of DNPs functionalized with linear molecules to differences in the radial extent and flexibility of their charged groups.

Dynamics of SUV−DNP Complex Elucidated by ^{31}P-T_2 Relaxation. To understand the surface functionalization of DNAs impacting the interactions with SUV membranes, we analyzed the dynamics of the POPG/POPC SUVs before and after exposure to amino DNPs using ^{31}P- T_2 relaxation NMR. We chose ^{31}P-NMR to characterize DNP−SUV complexes for two reasons. First, sample preparation is straightforward for this set of experiments and no further separation of the DNPs from the SUVs is needed, since ^{31}P nuclei are present only in the POPG and POPC lipids. Second, ^{31}P-T_2 NMR allowed us to directly probe dynamic changes of the phospholipids in SUVs upon exposure to DNPs.[36−38] The T_2 relaxation time is the time required for the transverse magnetization to lose coherence.[36,39] In liquids with fast, isotropic tumbling, T_2 approaches T_1, the time for the magnetization to return to longitudinal equilibrium.[39] However, in constrained environments, T_2 is sensitive to how restricted the motion is, due to spin−spin (primarily magnetic dipole−dipole) interactions.[36,39] Smaller T_2 values (broader line widths) indicate more restricted motions, and larger T_2 values (narrower line widths) indicate less restricted.

Figure 3a shows the 1D ^{31}P spectrum of the untreated SUVs, and Figure 3b−f shows the spectra of the SUVs after exposure

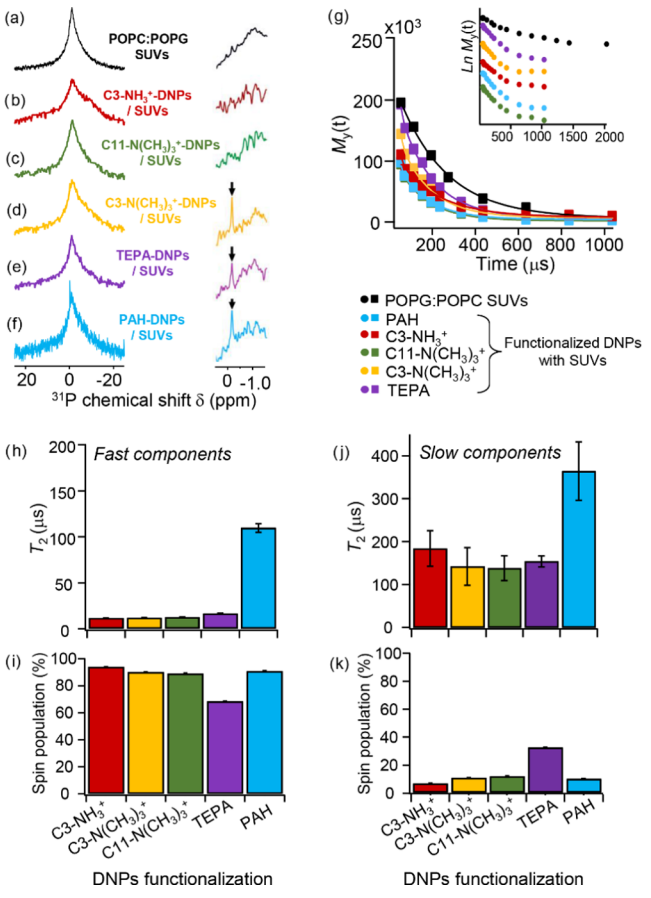

Figure 3. ^{31}P-NMR spectra of (a) POPC/POPG SUVs without DNP exposure and POPC/POPG SUVs upon exposure of (b) C3-NH_3^+-DNPs, (c) C11-N$(CH_3)_3^+$-DNPs, (d) C3-N$(CH_3)_3^+$-DNPs, (e) TEPA−DNPs, and (f) PAH−DNPs. (g) ^{31}P-T_2-NMR exponential decay curves of samples in (a)−(f) versus time. The inset in (g) shows the natural logarithm of the exponential decay, with individual plots offset vertically to eliminate overlap. The biexponential components of the T_2 times and their corresponding spin population in each sample are plotted in panels (h)−(k).

to functionalized nanodiamonds; also included here are spectra on an expanded scale showing near 0 ppm chemical shift. While ^{31}P-NMR spectra of the individual POPG and POPC ligands in water exhibit very narrow peaks with a full width at half-maximum (FWHM) of ~0.14 ppm (Supporting Information Figure S5), the ^{31}P spectra from the POPG/POPC bilayer are significantly broadened, with a peak width of 4.5 ppm (FWHM). Previous studies of multicomponent SUVs observed chemical shifts of several ppm between different phospholipids;[40] our spectra reveal only a single peak in the spectra of the SUVs (Figure 3a), suggesting that the phosphate groups in POPG and POPC and in both outer and inner monolayers are in similar environments that are not clearly distinguishable. This peak broadening arises from both heterogeneity in the

https://doi.org/10.1021/acs.langmuir.1c01146
Langmuir XXXX, XXX, XXX−XXX

Table 2. ^{31}P-T_2 Relaxation Results of Untreated POPC/POPG SUVs and Five Amino-Functionalized DNP-Treated SUVs[a]

	dynamic region 1 (more rigid motion)		dynamic region 2 (more flexible motion)	
	T_2 (μs)	population (%)	T_2 (μs)	population (%)
POPC/POPG vesicle	125.4 ± 11.8	48.1 ± 0.3	500.1 ± 86.4	51.9 ± 1.1
C3-NH_3^+-DNPs	10.9 ± 0.5	93.6 ± 0.3	183.8 ± 41.5	6.4 ± 0.1
C3-$N(CH_3)_3^+$-DNPs	11.6 ± 0.3	89.8 ± 0.3	142.0 ± 44.1	10.2 ± 0.2
C11-$N(CH_3)_3^+$-DNPs	12.0 ± 0.5	88.8 ± 0.4	138.2 ± 28.8	11.3 ± 0.5
TEPA−DNPs	16.1 ± 0.5	68.2 ± 0.2	153.7 ± 12.9	31.9 ± 0.3
PAH−DNPs	109.4 ± 4.6	90.4 ± 0.5	364.6 ± 68.4	9.6 ± 0.3

[a]All errors were obtained from regression analysis.

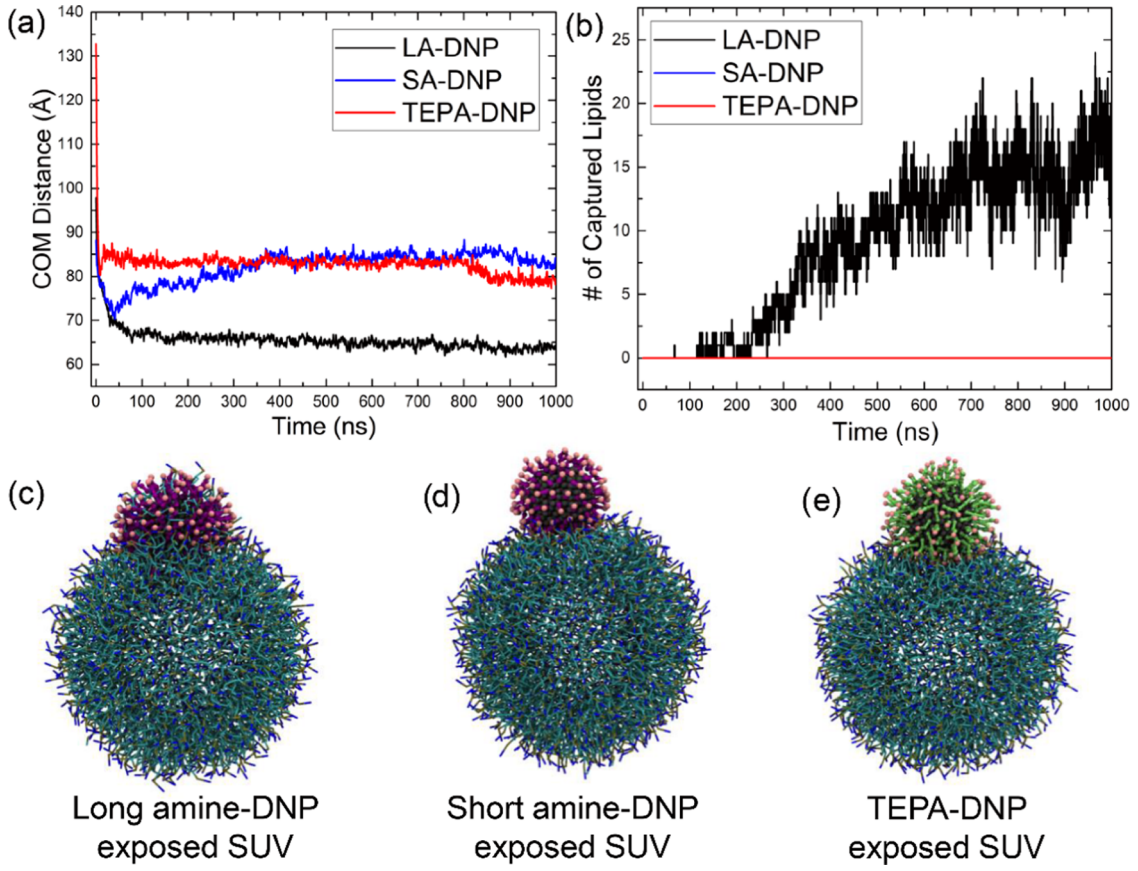

Figure 4. (a) Plots of the distance from the center of mass (COM) of SUV to the center of mass of 3-beads long amine-functionalized DNPs (black, LA−DNPs), 1-bead short amine-functionalized DNPs (blue, SA−DNPs), and TEPA−DNPs (red). (b) Plots of the number of captured lipids by the molecular ligand-functionalized DNPs. Snapshots of the interactions between an SUV and (c) LA−DNPs, (d) SA−DNPs, and (e) TEPA−DNPs. The snapshots were taken by the end of the simulation, and water molecules are not shown.

local environment and also decreases in spin coherence times due to strong dipolar interactions between motion-restricted, closely packed lipids in the vesicle walls.[41,42] The SUVs that were exposed to amino-functionalized DNPs (Figure 3b−f) show further line broadening (from 5.0 ppm to 8.7 ± 1.9 ppm FWHM) and a small shoulder at −9 ppm. Previous studies have shown that line broadening occurs and is sensitive to mobility[39,43,44] or symmetry[40] changes of the lipids from SUV complexes. Consequently, we attribute the additional broadening induced by interaction with the functionalized nanodiamond to a combination of decreased mobility of the lipids in the SUV and alterations in the chemical environment, such as the formation of complexes due to binding of nanoparticles to the SUVs.[45] While most samples exhibit primarily a single peak with an additional broad structure, SUVs that were exposed to DNPs functionalized with the PAH, TEPA, or C3-$N(CH_3)_3^+$ ligands clearly show a small but very narrow component (~1% spin population) in addition to a broadened peak. The presence of this narrow peak shows that there are free lipids in solution, thereby indicating that DNPs modified with these three ligands disrupt the SUV membranes and release free lipids into solution.

While the NMR ^{31}P line widths show that there are significant direct NP−SUV interactions, from these spectra alone, it is difficult to separate the contribution of heterogeneous broadening due to multiple chemical configurations from that of homogeneous broadening due to reduced spin coherent (T_2) times. We therefore measure the T_2 relaxation times of SUVs that were exposed to the different amino-functionalized DNPs. Figure 3g shows plots of magnetization vs time for the different samples, while the inset to Figure 3g shows the same data on a semilogarithmic plot. The

https://doi.org/10.1021/acs.langmuir.1c01146
Langmuir XXXX, XXX, XXX−XXX

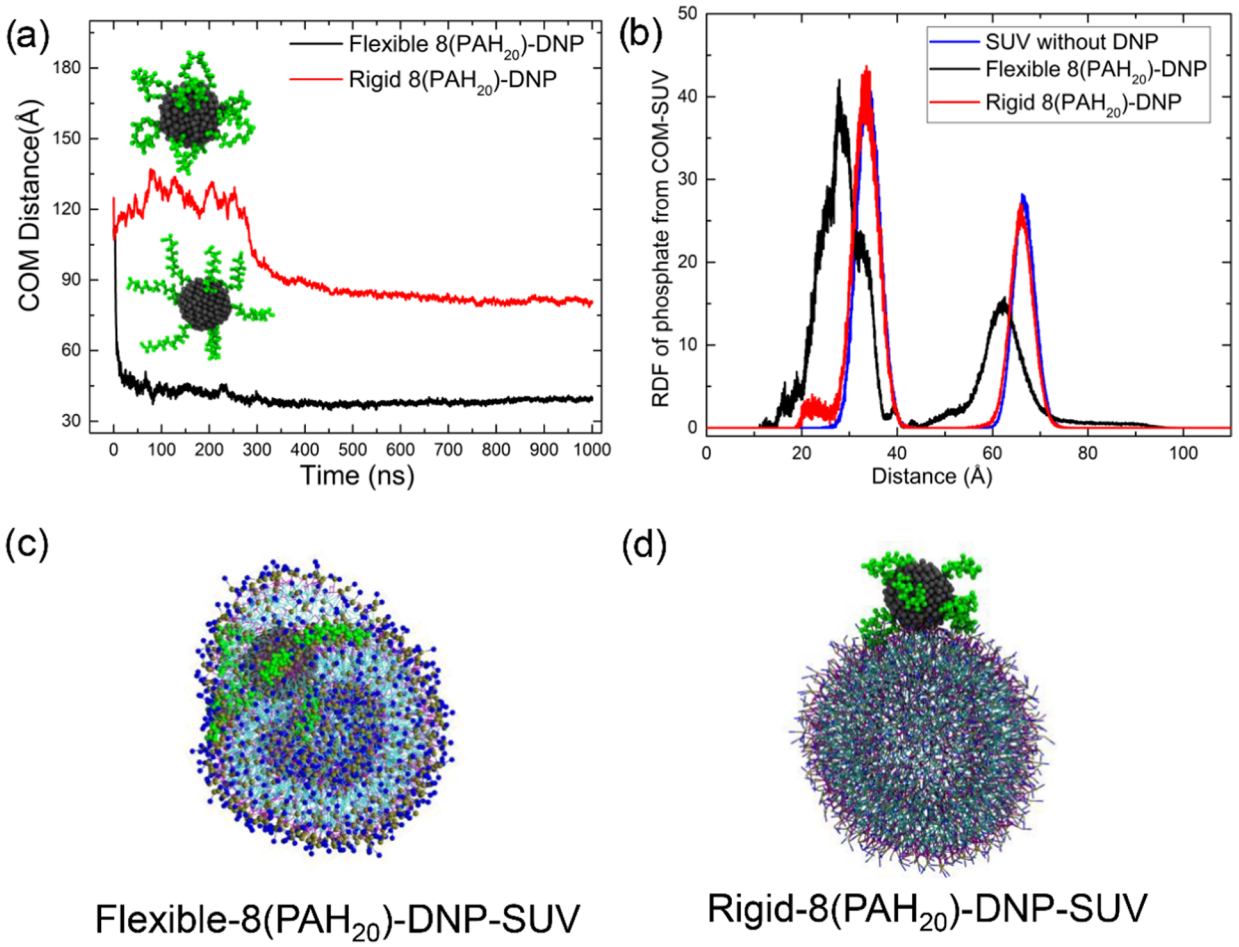

Figure 5. (a) Plots of the distance from the center of mass (COM) of SUV to the center of mass of 8(PAH_{20})−DNP during the MD simulation; in flexible PAH−DNP (black), each PAH chain has one end anchored to the DNP surface, while in rigid PAH−DNP (red), both ends of the PAH chain are anchored to the DNP surface. The inset shows the coarse-grained models for the rigid PAH−DNP (top) and flexible PAH−DNP (bottom). (b) Radial distribution function of phosphate with respect to the COM of SUV for the cases of SUV only (blue), exposed to flexible PAH−DNP (black), and exposed to rigid PAH−DNP (red). Snapshots of the interactions between SUV and (c) flexible PAH−DNPs and (d) rigid PAH−DNPs.

inset demonstrates clearly that the curves are biexponential, exhibiting two distinct regions: one below ∼400 μs and one at longer times. We fit these data in each region to obtain the different T_2 values and their corresponding spin populations, which are summarized in Table 2 and Figure 3h−k.

For POPC/POPG SUVs without amino DNPs, the inner phospholipids that are encapsulated inside the SUVs are expected to show less mobility compared to outer phospholipids.[46] For example, our MD simulations show that phospholipids in the inner membranes have diffusion coefficients almost half of those in the outer layers (Supporting Information). Based on these computational results, we attribute the longer (less motionally restricted) T_2 components (500.1 ± 86.4 μs) to the outer-layer phospholipids and the shorter (more motionally restricted) T_2 components (125.4 ± 11.8 μs) to the inner-layer phospholipids. The ratio of ^{31}P populations for these two T_2 components is 1:1, which is consistent with the assumption of a nearly identical number of molecules in the inner and outer membranes of the SUV.

Our data show that on exposure to functionalized DNPs, the ^{31}P-T_2 times are generally reduced compared to those for the intact SUVs. For all molecular-amino DNPs, two T_2 components were observed; a reduction in T_2 demonstrates that the SUVs increase when interacting with DNPs. Furthermore, the spin population analysis shows that the majority of the phospholipids in the SUVs (∼85%) exhibit fast relaxation (∼12.7 μs), suggesting they are in a highly restricted geometry. Surprisingly, the specific identity of the cationic amino groups and the length of the molecular-amino have little effect, as DNPs functionalized with molecular-amino groups all show similar T_2 values. DNPs functionalized with the polymeric amino groups (PAH−ND) also exhibit two T_2 components; however, the magnitude of reduction in the T_2 values is substantially smaller than that exhibited by SUVs exposed to molecular-amino DNPs, suggesting that the SUVs increase only slightly in rigidity.

Taken together with the fluorescence-based lysis assay results, our data show that the interactions between SUVs and molecular-amino DNPs are different from those between SUVs and polyamine−DNPs, and the degree of membrane damage is correlated to the overall mobility of the phospholipid. If lipid membranes lose integrity, the individual phospholipids are likely loosely packed and thus more mobile. Vice versa, if membranes maintain their integrity, the individual phospholipids are more rigid due to ordered packing. We thus propose that the rigid lipid motions in the presence of molecular-amino

https://doi.org/10.1021/acs.langmuir.1c01146
Langmuir XXXX, XXX, XXX−XXX

DNPs result from a strong association of these DNPs at the SUV surface and that the less restricted lipid motions upon interacting with polyamine PAH−DNPs result from the latter's ability to induce rearrangement or repacking of the phospholipids within SUVs.

Mechanistic Insights into DNP−SUV Interactions Using MD Simulation. To investigate in more molecular detail the different interactions between amino-functionalized DNP and SUV tests, we conducted coarse-grained molecular dynamics simulations. We aim to understand how the dynamics of the phospholipids from the SUV change upon interactions with polymer-functionalized DNP versus molecular ligand-functionalized DNP.

Figure 4a plots the evolution of the distance between the centers of mass (COM) of SUV and DNPs functionalized with molecular ligands during the MD simulation. The results show clearly that the DNP functionalized with long linear amines (LA−DNP) interacts more favorably with the SUV and adsorbs deeply into the phospholipid layer, as shown in the snapshot in Figure 4c. On the other hand, DNP functionalized with short linear amines (SA) exhibits much longer COM separation with the SUV (Figure 4a) and thus interacts much less with the phospholipid layer. This result demonstrates that SA−DNP only adsorbs at the SUV surface and induces much shallower penetration into the phospholipid layer, as shown in Figure 4d. The TEPA−DNP also adsorbs at the SUV surface with limited interactions with the phospholipid bilayer, as in Figure 4e. Since each TEPA carries twice as much charge as an SA or LA ligand (Table 1), the simulations show that the charge density of the surface ligand studied here does not play a major role in determining the DNP interactions with SUV. Furthermore, we simulated the ability of these DNPs to extract and capture lipids from the SUV over time. As shown in Figure 4b, the results show that only the long linear amine-DNP captures lipids from the SUV over time, while short linear amine-DNP and TEPA−DNP do not extract or capture lipids from the SUV. We attribute the differential behavior in lipid extraction to the length of the hydrophobic segment in these molecular ligands. A long linear amine has a long hydrophobic segment that packs with the hydrophobic lipid chains favorably, resulting in strong interactions with the phospholipid membrane, deeper penetration, and lipid extraction. By contrast, the hydrophobic section in SA is too short to have favorable packing with the SUV, resulting in weaker interactions with the phospholipid membrane, surface adsorption only, and no lipid extraction. Along this line, we note that the TEPA model used in the simulations does not feature the hydrophobic linker as in the experimental system, which likely explains the observation that TEPA−DNP behaves more similar to SA−DNP in the simulations.

Figure 5a plots the distance change between the centers of mass (COM) of SUV and PAH−DNP over time. As explained above, two different PAH−DNPs were simulated to examine the effect of chain flexibility on SUV−DNP interactions. The first model has one end of the PAH anchored to the DNP surface, which represents a PAH chain with a high degree of flexibility at the DNP surface (flexible PAH−DNP). The second PAH−DNP model has both ends of the PAH anchored to the DNP surface to form a loop, which represents a PAH chain with less flexibility (rigid PAH−DNP).

The results in Figure 5a show that both flexible PAH−DNP and rigid PAH−DNP adsorb readily to the SUV surface. While the rigid PAH−DNP shows similar COM distances to the SUV as the long amine-DNP over time, the flexible PAH−DNP exhibits much shorter COM distances to the SUV; i.e., the flexible PAH−DNP penetrates much deeper into the phospholipid bilayer than the rigid PAH−DNP. Furthermore, in Figure 5b, we show the radial distribution function of phosphate groups relative to the COM of the SUV before and after PAH−DNP exposure. With the flexible PAH−DNP model, significant shifts in lipid distribution (∼10 Å from the SUV without DNPs) are observed for both outer (∼70 Å) and inner (∼35 Å) lipid layers in the SUV. By contrast, much limited distribution shifts are observed with the rigid PAH−DNP model; we note that the direction of the peak shifts is less significant than the magnitude since the COM of SUV changes as it deforms. These results demonstrate that the phospholipid layers are much more perturbed by the flexible PAH−DNP than by the rigid PAH−DNP, leading to a higher degree of deformation of SUV, as also illustrated by the snapshots shown in Figure 5c,d.

Taken together, the MD simulations demonstrate that PAH−DNPs induce stronger interactions with the SUV membranes than the molecular ligand−DNPs (LA−DNP, SA−DNP, and TEPA−DNP). Furthermore, the flexibility of the PAH chain at the DNP surface plays an important role in controlling the NP−membrane interactions. PAH chains with higher flexibility lead to stronger interactions and penetrate deeply into the phospholipid layers, while PAH chains with higher rigidity lead to weaker interactions and only adsorption at the SUV surface. Finally, we have included simulations in the Supporting Information S.5, showing that increasing the number of PAH_{20} chains anchored on the DNP surface does not lead to deeper membrane penetration. This result again supports the notion that a higher surface charge density does not necessarily lead to a stronger interaction with phospholipid membranes.

Summary of DNP−SUV Interactions with Different Surface Ligands. Overall, our results reveal two major results. First, the fluorescence-based lysis assay normalized to amino concentration (Figure 2b) shows that on a per amine basis, each amino group of PAHs induces higher membrane damage than that of linear molecular ligands. Additionally, amino groups of long linear ligands induce higher membrane damage than that of short linear molecular ligands. These observations, along with our MD simulations, suggest that the concentration of surface-exposed amines at DNP surfaces is not the key to membrane damage, while the length of the hydrophobic segment and conformational flexibility of surface ligands are important. Second, T_2-NMR shows that all molecular ligand-functionalized DNPs induce significantly more rigid motions for ∼85% of the phospholipids in the SUV. By contrast, the mobility of the phospholipids remains rather high upon interaction with the PAH−DNPs. The T_2 results strongly suggest that the conformational flexibility of surface ligands plays a major role in determining the NP−membrane interactions. Our computational results further support the importance of ligand hydrophobic segment and ligand flexibility on NP−membrane interactions. Only long amine ligands were observed to extract lipids out of the SUV membrane, and while rigid PAH−DNP binds to the SUV surface with no membrane penetration, flexible PAH−DNP penetrates into the phospholipid bilayer and induces significant SUV deformation. To observe the actual membrane disruption, much longer simulations are required.

https://doi.org/10.1021/acs.langmuir.1c01146
Langmuir XXXX, XXX, XXX−XXX

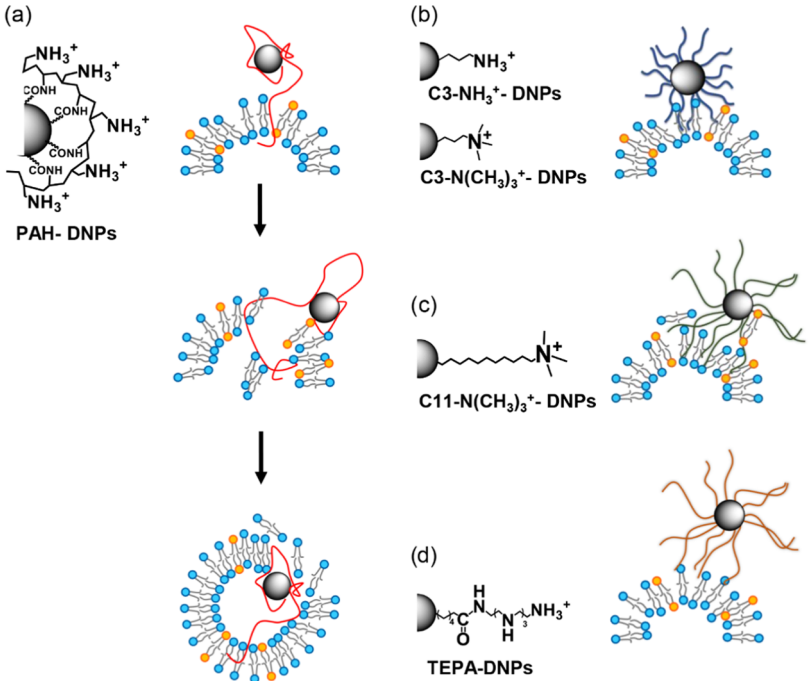

Figure 6. Illustration of proposed interactions between SUV membranes with polymer-functionalized (a) PAH−DNPs, molecular ligand-functionalized (b) C3-NH_3^+-DNPs, C3-$N(CH_3)_3^+$-DNPs, (c) C11-$N(CH_3)_3^+$-DNPs, and (d) TEPA−DNPs.

Taking the experimental and computational results together, we propose the qualitative descriptions for the DNP−SUV interactions with different surface ligands in Figure 6. The PAH−DNPs penetrate through phospholipid membranes and induce strong SUV deformation via the highly flexible PAH chains that are extending into the solution (Figure 6a); these mobile chains "wiggle" deeply into the membrane and induce phospholipid rearrangement. By contrast, the shorter molecular ligands pack tightly with the phospholipids in the SUV (Figure 6b−d), leading to fast T_2 relaxation, as observed experimentally (Table 2). The rigidity of the molecular ligands prevents them from penetrating deeply into the membrane, and the DNP remains bound to the SUV surface. Nevertheless, if the molecular ligands feature sufficiently long hydrophobic segments, they are able to extract lipids out of the membrane and lead to damage to the SUV. While demonstrated here for diamond nanoparticles intentionally functionalized with molecules with well-defined structures, similar considerations might also be expected to be important for nanoparticles with other coatings, such as biopolymers that form protein coronas.

CONCLUSIONS

To better control how functionalized nanomaterials impact biological systems, it is essential to understand the molecular factors that dictate the nano/biointeractions. With a combination of experimental and computational studies, we demonstrate here that while cationic surface ligands feature favorable electrostatic interactions with anionic phospholipid membranes, the length of the hydrophobic segment and conformational flexibility of ligands at nanoparticle surfaces play critical roles in modulating the strength of such interactions. Our work shows that the membrane deformation and damage are the greatest when the molecular functional groups form flexible chains/tails, extending away from the nanoparticle core. Flexible chains induce greater membrane deformation and deeper penetration, while rigid molecular ligands lead to surface adsorption only. While in some environments nanoparticles might be expected to be coated with proteins or other biopolymers in the form of a protein corona, we anticipate that similar structural and conformational properties of molecules forming coronas will also affect how nanoparticles with different coronas induce distinct biological responses. This work provides additional insights into the factors that govern the interactions between functionalized NPs and lipid membranes, and the results can be used to better design nanomaterials for specific effects on the cell membrane.

ASSOCIATED CONTENT

Supporting Information

The Supporting Information is available free of charge at https://pubs.acs.org/doi/10.1021/acs.langmuir.1c01146.

Experimental data of surface characterization of different cationic-functionalized DNPs, fluorescence-based lysis assay plot versus diamond NP concentration, ^{1}H-T_2 NMR analysis of PAH−DNPs, 1D−^{31}P-NMR spectra of POPC, POPG lipid control; and the MD simulation results of diffusion coefficients of lipids in SUVs, ligand density, and bead type on DNP cores (PDF)

AUTHOR INFORMATION

Corresponding Author

Robert J. Hamers − *Department of Chemistry, University of Wisconsin-Madison, Madison, Wisconsin 53706, United States*; orcid.org/0000-0003-3821-9625; Email: rjhamers@wisc.edu

Authors

Yongqian Zhang − *Department of Chemistry, University of Wisconsin-Madison, Madison, Wisconsin 53706, United States*

https://doi.org/10.1021/acs.langmuir.1c01146
Langmuir XXXX, XXX, XXX−XXX

Udaya Dahal − *Department of Chemistry, Boston University, Boston, Massachusetts 02215, United States*
Z. Vivian Feng − *Chemistry Department, Augsburg University, Minneapolis, Minnesota 55454, United States;* orcid.org/0000-0002-3329-3781
Zeev Rosenzweig − *Department of Chemistry, University of Maryland Baltimore County, Baltimore, Maryland 21250, United States;* orcid.org/0000-0001-6098-3932
Qiang Cui − *Department of Chemistry, Boston University, Boston, Massachusetts 02215, United States;* orcid.org/0000-0001-6214-5211

Complete contact information is available at: https://pubs.acs.org/10.1021/acs.langmuir.1c01146

Author Contributions

[⊥]Y.Z. and U.D. contributed equally.

Funding

National Science Foundation, Mathematical and Physical Sciences Directorate, Division of Chemistry, CHE-2001611 National Institutes of Health, S10OD012245.

Notes

The authors declare no competing financial interest.

■ ACKNOWLEDGMENTS

This work was supported by the NSF Center for Sustainable Nanotechnology, CHE-2001611. The Center for Sustainable Nanotechnology is part of the Centers for Chemical Innovation Program. The Bruker Avance 600 NMR instrument used in this work was supported by the National Institutes of Health grants S10OD012245. The authors thank Dr. Charles G. Fry for suggestions regarding the manuscript and Zheng Zheng (University of Maryland Baltimore County) for valuable training for fluorescence-based lysis experiments.

■ REFERENCES

(1) Verma, A.; Stellacci, F. Effect of surface properties on nanoparticle−cell interactions. *Small* **2010**, *6*, 12−21.
(2) Cho, E. C.; Xie, J.; Wurm, P. A.; Xia, Y. Understanding the Role of Surface Charges in Cellular Adsorption versus Internalization by Selectively Removing Gold Nanoparticles on the Cell Surface with a I2/KI Etchant. *Nano Lett.* **2009**, *9*, 1080−1084.
(3) Feng, Z. V.; Gunsolus, I. L.; Qiu, T. A.; Hurley, K. R.; Nyberg, L. H.; Frew, H.; Johnson, K. P.; Vartanian, A. M.; Jacob, L. M.; Lohse, S. E.; Torelli, M. D.; Hamers, R. J.; Murphy, C. J.; Haynes, C. L. Impacts of gold nanoparticle charge and ligand type on surface binding and toxicity to Gram-negative and Gram-positive bacteria. *Chem. Sci.* **2015**, *6*, 5186−5196.
(4) Leroueil, P. R.; Berry, S. A.; Duthie, K.; Han, G.; Rotello, V. M.; McNerny, D. Q.; Baker, J. R.; Orr, B. G.; Banaszak Holl, M. M. Wide Varieties of Cationic Nanoparticles Induce Defects in Supported Lipid Bilayers. *Nano Lett.* **2008**, *8*, 420−424.
(5) Xie, X.; Liao, J.; Shao, X.; Li, Q.; Lin, Y. The Effect of shape on Cellular Uptake of Gold Nanoparticles in the forms of Stars, Rods, and Triangles. *Sci. Rep.* **2017**, *7*, No. 3827.
(6) Thomas, M.; Klibanov, A. M. Enhancing polyethylenimine's delivery of plasmid DNA into mammalian cells. *Proc. Natl. Acad. Sci. U.S.A.* **2002**, *99*, 14640−14645.
(7) Sakagami, K.; Masuda, T.; Kawano, K.; Futaki, S. Importance of Net Hydrophobicity in the Cellular Uptake of All-Hydrocarbon Stapled Peptides. *Mol. Pharmaceutics* **2018**, *15*, 1332−1340.
(8) Hu, Y.; Xie, J.; Tong, Y. W.; Wang, C.-H. Effect of PEG conformation and particle size on the cellular uptake efficiency of nanoparticles with the HepG2 cells. *J. Controlled Release* **2007**, *118*, 7−17.
(9) Verma, A.; Uzun, O.; Hu, Y.; Hu, Y.; Han, H.-S.; Watson, N.; Chen, S.; Irvine, D. J.; Stellacci, F. Surface-structure-regulated cell-membrane penetration by monolayer-protected nanoparticles. *Nat. Mater.* **2008**, *7*, 588−595.
(10) Ackerson, C. J.; Sykes, M. T.; Kornberg, R. D. Defined DNA/nanoparticle conjugates. *Proc. Natl. Acad. Sci. U.S.A.* **2005**, *102*, 13383−13385.
(11) Stobiecka, M.; Deeb, J.; Hepel, M. Ligand exchange effects in gold nanoparticle assembly induced by oxidative stress biomarkers: Homocysteine and cysteine. *Biophys. Chem.* **2010**, *146*, 98−107.
(12) Perera, G. S.; Athukorale, S. A.; Perez, F.; Pittman, C. U., Jr; Zhang, D. Facile displacement of citrate residues from gold nanoparticle surfaces. *J. Colloid Interface Sci.* **2018**, *511*, 335−343.
(13) Yang, W.; Auciello, O.; Butler, J. E.; Cai, W.; Carlisle, J. A.; Gerbi, J. E.; Gruen, D. M.; Knickerbocker, T.; Lasseter, T. L.; Russell, J. N.; Smith, L. M.; Hamers, R. J. DNA-modified nanocrystalline diamond thin-films as stable, biologically active substrates. *Nat. Mater.* **2002**, *1*, 253−257.
(14) Stavis, C.; Clare, T. L.; Butler, J. E.; Radadia, A. D.; Carr, R.; Zeng, H.; King, W. P.; Carlisle, J. A.; Aksimentiev, A.; Bashir, R. Surface functionalization of thin-film diamond for highly stable and selective biological interfaces. *Proc. Natl. Acad. Sci. U.S.A.* **2011**, *108*, 983−988.
(15) Krueger, A.; Lang, D. Functionality is key: recent progress in the surface modification of nanodiamond. *Adv. Funct. Mater.* **2012**, *22*, 890−906.
(16) Zhang, Y.; Tamijani, A. A.; Taylor, M. E.; Zhi, B.; Haynes, C. L.; Mason, S. E.; Hamers, R. J. Molecular Surface Functionalization of Carbon Materials via Radical-Induced Grafting of Terminal Alkenes. *J. Am. Chem.Soc.* **2019**, *141*, 8277−8288.
(17) Zhang, Y.; Hudson-Smith, N. V.; Frand, S. D.; Cahill, M. S.; Davis, L. S.; Feng, Z. V.; Haynes, C. L.; Hamers, R. J. Influence of the Spatial Distribution of Cationic Functional Groups at Nanoparticle Surfaces on Bacterial Viability and Membrane Interactions. *J. Am. Chem. Soc.* **2020**, *142*, 10814−10823.
(18) Edidin, M. Lipids on the frontier: a century of cell-membrane bilayers. *Nat. Rev. Mol. Cell Biol.* **2003**, *4*, 414−418.
(19) Moghadam, B. Y.; Hou, W.-C.; Corredor, C.; Westerhoff, P.; Posner, J. D. Role of nanoparticle surface functionality in the disruption of model cell membranes. *Langmuir* **2012**, *28*, 16318−16326.
(20) Chen, K. L.; Bothun, G. D. Nanoparticles Meet Cell Membranes: Probing Nonspecific Interactions using Model Membranes. *Environ. Sci. Technol.* **2014**, *48*, 873−880.
(21) Zhang, X.; Pandiakumar, A. K.; Hamers, R. J.; Murphy, C. J. Quantification of Lipid Corona Formation on Colloidal Nanoparticles from Lipid Vesicles. *Anal. Chem.* **2018**, *90*, 14387−14394.
(22) Zheng, Z.; Saar, J.; Zhi, B.; Qiu, T. A.; Gallagher, M. J.; Fairbrother, D. H.; Haynes, C. L.; Lienkamp, K.; Rosenzweig, Z. Structure−Property Relationships of Amine-rich and Membrane-Disruptive Poly(oxonorbornene)-Coated Gold Nanoparticles. *Langmuir* **2018**, *34*, 4614−4625.
(23) Kendall, D. A.; MacDonald, R. C. A fluorescence assay to monitor vesicle fusion and lysis. *J. Biol. Chem.* **1982**, *257*, 13892−13895.
(24) Marrink, S. J.; Risselada, H. J.; Yefimov, S.; Tieleman, D. P.; de Vries, A. H. The MARTINI Force Field: Coarse Grained Model for Biomolecular Simulations. *J. Phys. Chem. B* **2007**, *111*, 7812−7824.
(25) Das, M.; Dahal, U.; Mesele, O.; Liang, D.; Cui, Q. Molecular Dynamics Simulation of Interaction between Functionalized Nanoparticles with Lipid Membranes: Analysis of Coarse-Grained Models. *J. Phys. Chem. B* **2019**, *123*, 10547−10561.
(26) Krueger, A. New Carbon Materials: Biological Applications of Functionalized Nanodiamond Materials. *Chem. - Eur. J.* **2008**, *14*, 1382−1390.
(27) Jo, S.; Kim, T.; Iyer, V. G.; Im, W. CHARMM-GUI: A web-based graphical user interface for CHARMM. *J. Comput. Chem.* **2008**, *29*, 1859−1865.

(28) Vogel, R.; Pal, A. K.; Jambhrunkar, S.; Patel, P.; Thakur, S. S.; Reátegui, E.; Parekh, H. S.; Saá, P.; Stassinopoulos, A.; Broom, M. F. High-Resolution Single Particle Zeta Potential Characterisation of Biological Nanoparticles using Tunable Resistive Pulse Sensing. *Sci. Rep.* **2017**, *7*, No. 17479.
(29) Domínguez, G. A.; Torelli, M. D.; Buchman, J. T.; Haynes, C. L.; Hamers, R. J.; Klaper, R. D. Size dependent oxidative stress response of the gut of Daphnia magna to functionalized nanodiamond particles. *Environ. Res.* **2018**, *167*, 267−275.
(30) Zhang, Y.; Fry, C. G.; Pedersen, J. A.; Hamers, R. J. Dynamics and Morphology of Nanoparticle-Linked Polymers Elucidated by Nuclear Magnetic Resonance. *Anal. Chem.* **2017**, *89*, 12399−12407.
(31) Blum, F. D.; Xu, G.; Liang, M.; Wade, C. G. Dynamics of Poly (vinyl acetate) in Bulk and on Silica. *Macromolecules* **1996**, *29*, 8740−8745.
(32) Lin, W.-Y.; Blum, F. D. Segmental dynamics of bulk and silica-adsorbed poly (methyl acrylate)-d 3 by deuterium NMR: the effect of molecular weight. *Macromolecules* **1998**, *31*, 4135−4142.
(33) Blum, F. D. Magnetic resonance of polymers at surfaces. *Colloids Surf.* **1990**, *45*, 361−376.
(34) Cosgrove, T.; Griffiths, P.; Lloyd, P. Polymer adsorption. The effect of the relative sizes of polymer and particle. *Langmuir* **1995**, *11*, 1457−1463.
(35) Hershkovits, E.; Tannenbaum, A.; Tannenbaum, R. Polymer adsorption on curved surfaces: a geometric approach. *J. Phys. Chem. C* **2007**, *111*, 12369−12375.
(36) Levitt, M. H. *Spin dynamics: basics of nuclear magnetic resonance*; John Wiley & Sons, 2001; p 686.
(37) Summers, J. S.; Hoogstraten, C. G.; Britt, R. D.; Base, K.; Shaw, B. R.; Ribeiro, A. A.; Crumbliss, A. L. 31P NMR probes of chemical dynamics: paramagnetic relaxation enhancement of the 1H and 31P NMR resonances of methyl phosphite and methylethyl phosphate anions by selected metal Complexes. *Inorg. Chem.* **2001**, *40*, 6547−6554.
(38) Bogner, W.; Chmelik, M.; Schmid, A. I.; Moser, E.; Trattnig, S.; Gruber, S. Assessment of 31P relaxation times in the human calf muscle: A comparison between 3 T and 7 T in vivo. *Magn. Reson. Med.* **2009**, *62*, 574−582.
(39) Claridge, T. D. W. *High-Resolution NMR Techniques in Organic Chemistry*, 3rd ed.; Elsevier: 2016; p 541.
(40) Traïkia, M.; Warschawski, D. E.; Lambert, O.; Rigaud, J.-L.; Devaux, P. F. Asymmetrical membranes and surface tension. *Biophys. J.* **2002**, *83*, 1443−1454.
(41) Janosi, L.; Gorfe, A. A. Simulating POPC and POPC/POPG bilayers: conserved packing and altered surface reactivity. *J. Chem. Theory. Comput.* **2010**, *6*, 3267−3273.
(42) Filippov, A. V.; Khakimov, A. M.; Munavirov, B. V. 31P NMR Studies of Phospholipids. In *Annual Reports on NMR Spectroscopy*; Elsevier, 2015; Vol. *85*, pp 27−92.
(43) Hens, Z.; Martins, J. C. A solution NMR toolbox for characterizing the surface chemistry of colloidal nanocrystals. *Chem. Mater.* **2013**, *25*, 1211−1221.
(44) Riccardi, L.; Gabrielli, L.; Sun, X.; De Biasi, F.; Rastrelli, F.; Mancin, F.; De Vivo, M. Nanoparticle-based receptors mimic protein-ligand recognition. *Chem.* **2017**, *3*, 92−109.
(45) Yang, Y.; Yao, H.; Hong, M. Distinguishing Bicontinuous Lipid Cubic Phases from Isotropic Membrane Morphologies Using 31P Solid-State NMR Spectroscopy. *J. Phys. Chem. B* **2015**, *119*, 4993−5001.
(46) Wong, T. C. Micellar systems: Nuclear Magnetic Resonance Spectroscopy. In *Encyclopedia of Surface and Colloid Science*, 2006; Vol. *5*, p 3742.

https://doi.org/10.1021/acs.langmuir.1c01146
Langmuir XXXX, XXX, XXX−XXX